

Decoupling Optical and Thermal Responses: Thermo-optical Nonlinearities Unlock MHz Transmission Modulation in Dielectric Metasurfaces

Omer Can Karaman, Gopal Narmada Naidu, Alan R. Bowman, Elif Nur Dayi and Giulia Tagliabue*

Laboratory of Nanoscience for Energy Technologies (LNET), STI, École Polytechnique Fédérale de Lausanne, 1015 Lausanne, Switzerland

December 3, 2024

Abstract

Thermo-optical nonlinearities (TONL) in metasurfaces enable dynamic control of optical properties like transmission, reflection, and absorption through external stimuli such as laser irradiation or temperature. As slow thermal dynamics of extended systems are expected to limit modulation speeds ultimately, research has primarily focused on steady-state effects. In this study, we investigate photo-driven TONL in amorphous silicon (a-Si) metasurfaces both under steady-state and, most importantly, dynamic conditions (50 kHz modulation) using a 488 nm continuous-wave pump laser. First, we show that a non-monotonic change in the steady-state transmission occurs at wavelengths longer than the electric-dipole resonance (800 nm). In particular, at 815 nm transmission first decreases by 30% and then increases by 30% as the laser intensity is raised to $5 \text{ mW}/\mu\text{m}^2$. Next, we demonstrate that TONL decouple the thermal and optical characteristic times, the latter being up to 7 times shorter in the tested conditions (i.e. $\tau_{opt} = 0.5 \mu\text{s}$ vs $\tau_{th} = 3.5 \mu\text{s}$). Most remarkably, we experimentally demonstrate that combining these two effects enables optical modulation at twice the speed (100 kHz) of the excitation laser modulation. We finally show how to achieve all-optical transmission modulation at MHz speeds with large amplitudes (85%). Overall, these results show that photo-driven TONL produce large and fully reversible transmission modulation in dielectric metasurfaces with fast and adjustable speeds. Therefore, they open completely new opportunities toward exploiting TONL in dynamically reconfigurable systems, from optical switching to wavefront manipulation.

1 Introduction

Tunable metasurfaces are of great importance in the fields of optics and photonics due to their ability to manipulate electromagnetic waves across a wide range of frequencies[1, 2]. Unlike traditional static optical elements, tunable metasurfaces offer flexibility in real-time control of properties such as phase, amplitude, and polarization of light [3, 4, 5, 6, 7]. The mechanisms of tunability in active metasurfaces generally involve external stimuli such as electrical, optical, mechanical, or thermal inputs that alter the material's optical properties. Electro-refractive tuning is primarily achieved by integrating materials with high electro-optic coefficients, such as liquid crystals[8], III-V semiconductors [9] or lithium niobate (LN), [10], into the metasurface design. Optical tuning, instead, is typically achieved by exploiting nonlinear optical effects, such as Kerr effect[11], or photo-induced processes, such as hot carriers generation in plasmonic metals[12, 13, 14] or free carrier generation in semiconductors [15].

Thermo-optical and photo-thermal nonlinearities have been widely explored recently for their potential in tuning optical responses in nanostructures and metasurfaces. Indeed metasurfaces exploiting Mie resonances in

*Correspondence email address: giulia.tagliabue@epfl.ch

high-refractive-index dielectric materials, such as silicon, can confine light efficiently and generate strong field enhancements within the nanoresonators. This is particularly valuable in enabling nonlinear optical phenomena in silicon, which are too weak in the bulk material [16, 17, 18, 19]. The ability to modulate light dynamically in such systems has implications for various advanced photonic applications, including optical switching [20], beam steering [21, 22, 23], and polarization manipulation [7, 5, 6]. In recent works exploring photo-thermal and thermo-optical nonlinearities, the focus has predominantly been on steady-state nonlinear behavior in silicon-based metasurfaces and nanostructures [17, 24]. These studies have demonstrated impressive modulation of the optical properties through both photo-thermal effects, where absorbed light induces heating, and thermo-optical effects, where temperature changes modify the refractive index. For example, silicon nanostructures have been shown to modulate scattering and transmission intensities under continuous-wave (CW) excitation, with effective nonlinear indices n_2 orders of magnitude higher than bulk silicon (i.e. $n = n_0 + n_2 I$ where I is the excitation intensity) [16, 25, 18]. Recently, the studies introduced quasi-bound states in the continuum, q-BIC, in silicon metasurfaces to enable thermo-optical bistability, and optimize hysteresis width and switching power, suggesting a path for energy-efficient optical computing and non-reciprocity using silicon-based metasurfaces [26, 27].

However, while steady-state studies have achieved significant breakthroughs, transient modulation through thermo-optical and photo-thermal nonlinearities has been thought to be inherently limited by the thermal response time of the system. This is particularly evident when photo-thermal effects, which involve localized heating and changes in the optical properties, are used for dynamic modulation [16]. Most metasurfaces and nanostructures investigated for their thermo-optical responses, such as those supporting high-Q resonances, are bound by the timescales required for heat diffusion, limiting their application in scenarios requiring fast modulation speeds [28, 29].

In this study, we investigate the photo-thermo-optical response and nonlinear dynamics of amorphous silicon (a-Si) metasurfaces (**Figure 1a**), demonstrating their unique capability to decouple thermal and optical characteristic timescale as well as their potential for photothermally-driven transmission modulation, both in terms of amplitude and speed. We designed and fabricated high-Q electric dipole resonant metasurfaces and characterized their transmission spectrum, $T(\lambda)$, where λ is the wavelength, under both steady-state and modulated (50 kHz) photo-excitation using a CW 488 nm laser with variable intensity and beam size. Under steady-state irradiation, we demonstrate large, nonlinear, and fully reversible changes in $T(\lambda)$, with both the sign (i.e., increase or decrease) and intensity dependence determined by the wavelength position relative to resonance. On resonance (i.e. 800 nm), a monotonic increase of T from 0.09 to 0.51 ($\approx 470\%$ experimental, $\approx 1360\%$ theoretical) is obtained under $5 \text{ mW}/\mu\text{m}^2$ irradiation. Strikingly, at 815 nm (red-shifted from resonance), a non-monotonic response is reported, with T first decreasing from to 0.22 (-31% at $1.5 \text{ mW}/\mu\text{m}^2$) and then increasing to 0.41 (+29% at $5 \text{ mW}/\mu\text{m}^2$). For modulated irradiation, we further show that thermo-optical non-linearities (TONL) uniquely decouple the system's thermal response time (τ_{th}) from its optical response time (τ_{opt}) (**Fig. 1b**). For example, with a beam diameter of $3 \mu\text{m}$, exciting approximately 7 by 7 a-Si nanoresonators, the heating dynamics exhibit $\tau_{th,heat}$ (the time interval between 10% and 90% of the temperature change) $\approx 3.5 \mu\text{s}$, while the transmission, $T(t)$, response time decreases with increasing excitation intensity, reaching $\tau_{opt,heat}$ (the time interval between 10% and 90% of the transmission change) $\approx 0.5 \mu\text{s}$ at $3.3 \text{ mW}/\mu\text{m}^2$. Most remarkably, we demonstrate that the combination of non-monotonic $T(t)$ response and decoupled τ_{th}/τ_{opt} can lead to a doubling of the optical modulation frequency (100 kHz) with respect to the photothermal modulation frequency (50 kHz) while preserving a large modulation amplitude (30% experimental, 85% theoretical). Finally, we discuss how τ_{th}/τ_{opt} decoupling can also enable photo-thermo-optical modulation speeds exceeding 1 MHz. Our experimental findings are in excellent agreement with a Multiphysics COMSOL model, which incorporates newly measured, temperature-dependent refractive index (n) and extinction coefficient (k) data for a-Si over 20–220°C. Overall, these results highlight that photo-driven TONL in dielectric metasurfaces open completely new opportunities toward dynamically reconfigurable systems, including optical switching devices [20] and wavefront manipulation components, such as beam steering [22, 23] and metalenses [30, 31].

2 Results

Optical properties of the a-Si metasurface. We designed and fabricated a-Si metasurfaces consisting of an array of nanodisks with diameters (D) ranging from 200 nm to 300 nm, a height (H) of 100 nm and a periodicity (P) of 380 nm. The experimental transmission spectrum of the metasurface with nanodisks of 290 nm diameter

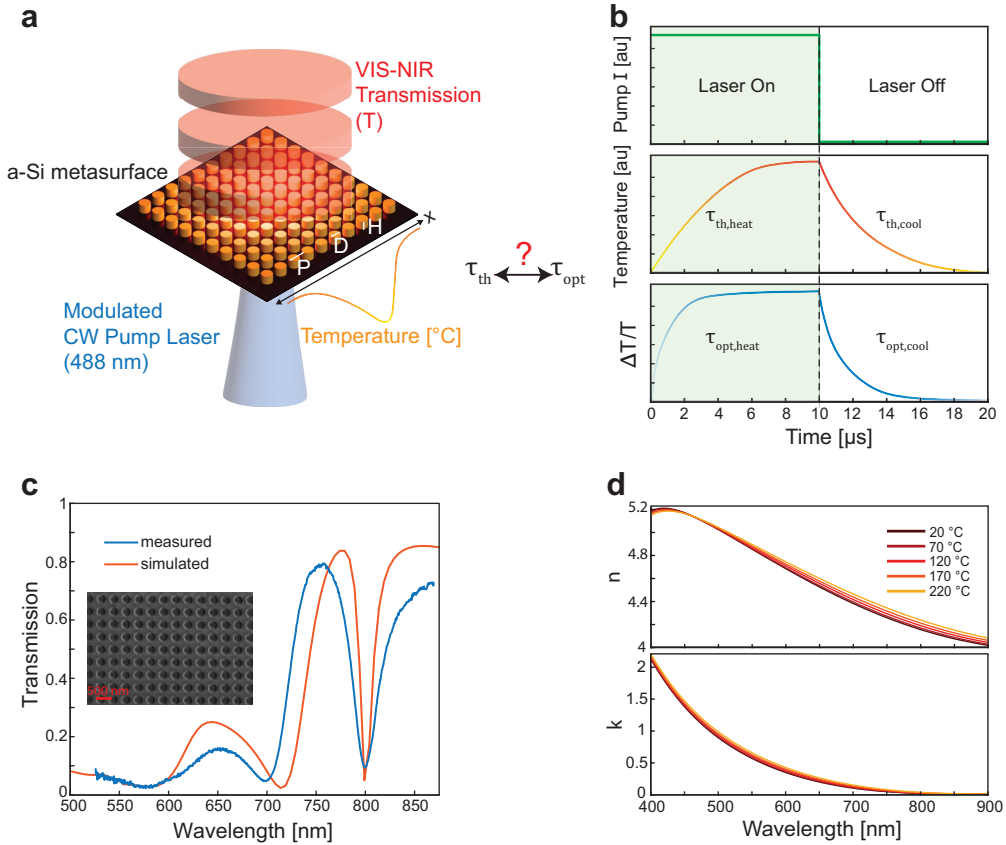


Figure 1: **Optical properties of the proposed a-Si metasurface.** **a** The schematic illustration of a-Si metasurface on Fused Silica substrate (P, D, and H denote the periodicity, diameter, and height of the disks, respectively.). **b** The schematic illustration of the modulated CW laser signal (upper), the temperature evolution in time (middle) and differential transient transmission (lower), $\Delta T/T$, of the metasurface. **c** The transmission spectra of the fabricated (blue) and simulated (orange) metasurfaces. The inset shows the SEM image of the fabricated metasurface with P of 380 nm, D of 290 nm, and H of 100 nm. **d** The measured real part, n , and imaginary part, k , of the refractive indices of a-Si at 20 °C, 70 °C, 120 °C, 170 °C, and 220 °C.

(**Fig. 1c**, blue curve) is characterized by two pronounced dips around 695 nm and 800 nm, in good agreement with the simulated results (orange curve). The resonance at 695 nm is attributed to the magnetic dipole (MD) mode, while the resonance at 800 nm corresponds to the electric dipole (ED) mode. We provide detailed field profiles for both the MD and ED resonances in **Supplementary Fig. 1**, illustrating the field confinement and mode distributions at these resonant wavelengths. The quality factor (Q -factor) of the experimental ED resonance at 800 nm is ≈ 50 , reflecting the metasurface’s ability to achieve strong light confinement and offer good possibility for optical modulation. This is made possible by the high quality of the fabricated nanodisk array (see inset of **Fig. 1c**). While there is a close agreement between the simulated and measured spectra, slight deviations are likely due to small fabrication imperfections or unaccounted material loss in the simulations. Nonetheless, both the experimental and simulated data confirm the strong resonant behavior of the metasurface within the visible to near-infrared spectrum, showcasing its potential for applications in optical modulation.

To further explore the thermo-optical properties of the metasurface, the temperature dependence of the refractive index of an a-Si thin film (100 nm thick) is measured by ellipsometry using an external heater to vary the sample temperature from 20 °C to 220 °C (**Fig. 1d**). The measurement shows that across the visible and near-infrared wavelength range, a-Si thermo-optical coefficient is dispersive and can be negative or positive depending on the wavelength (see **Supplementary Fig. 5**), differently from previously assumed constant values across the spectrum[32, 33, 34]. The real (n) and imaginary (k) parts of the refractive index of a-Si exhibit a

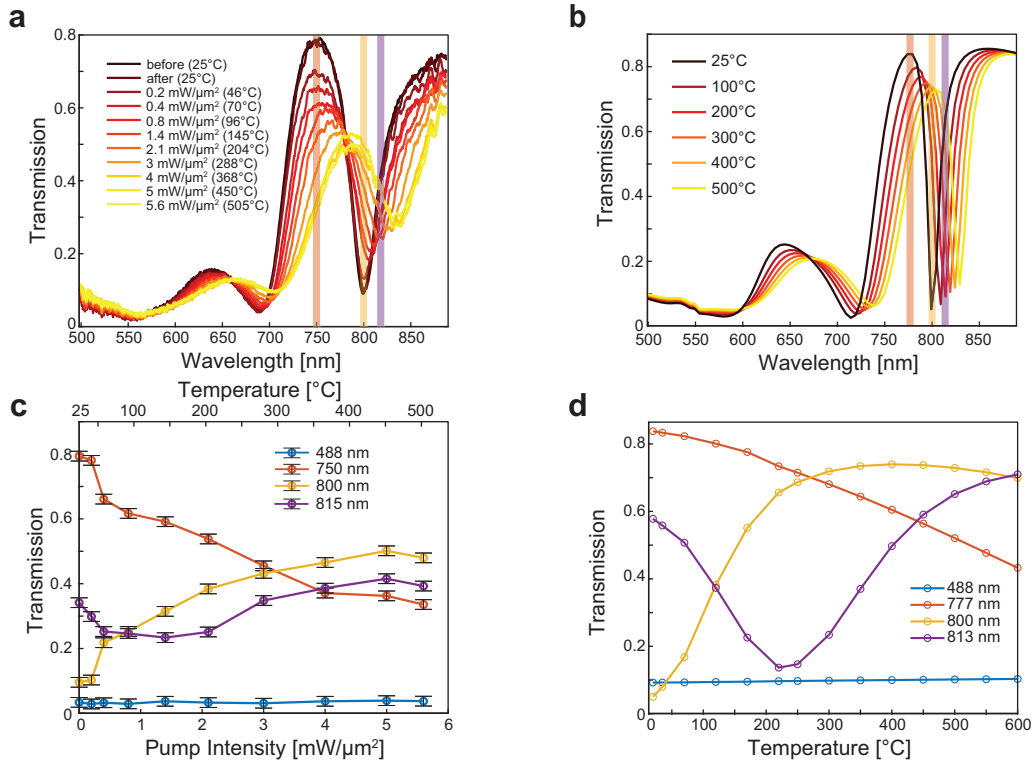


Figure 2: **The measured and simulated TONL in steady-state.** **a** The measured transmission spectra of the metasurface under different pump intensities. The legend specifies the temperatures measured by Raman thermometry at the corresponding pump intensities. The semi-transparent regions specify the probe wavelengths in **c**. **b** The simulated transmission spectra of the metasurface under different pump intensities. The semi-transparent regions specify the probe wavelengths in **d**. **c** The measured pump intensity-dependent transmission of the metasurface at the probe wavelengths of 488 nm (blue), 750 nm (orange), 800 nm (yellow), and 815 nm (violet). Upper x-axis shows the measured temperatures corresponding to the pump intensities. **d** The simulated pump intensity (temperature)-dependent transmission of the metasurface at the probe wavelengths of 488 nm (blue), 777 nm (orange), 800 nm (yellow), and 813 nm (violet).

more pronounced increase in the spectral window between 650 nm and 850 nm as the temperature increases. This temperature dependence reflects the thermo-optic effect in a-Si, which can be exploited to dynamically tune the optical properties of the metasurface under varying thermal conditions. Notably, the measured thermo-optical coefficient, derived from the variation of the refractive index (n) with temperature, exhibits a maximum ($\approx 4 \times 10^{-4} \text{ K}^{-1}$) at $\approx 800 \text{ nm}$, coinciding with the ED resonance (see **Supplementary Fig. 5a**). This alignment between the peak thermo-optical coefficient and the ED resonance highlights the metasurface as an ideal platform for exploring thermo-optical effects. The strong field confinement at the ED resonance further amplifies the temperature-induced refractive index changes, making it particularly suited for dynamic tuning of optical properties via thermal modulation. Note that our measurements reveal that the real part of the thermo-optical coefficient of a-Si is 0 at $\approx 480 \text{ nm}$, which makes this spectral region important for applications requiring high stability against temperature changes[35, 36].

TONL in steady-state optical response To explore the impact of TONL on the steady-state transmission spectrum of a-Si metasurfaces, we perform a series of transmission measurements under varying photoexcitation intensities (**Figure 2**). A 488 nm continuous wave (CW) laser is used as *pump* to photoexcite/heat the metasurface, which has an absorption of ≈ 0.55 at this wavelength. Simultaneously, a low-intensity, CW white light source is utilized as the *probe* to measure the transmission spectra across the visible/near-infrared spectrum, allowing us to quantify the change of the metasurface’s optical transmission in real-time at selected probe wavelengths. Further details of the experimental setup, including a diagram, are provided in the Methods section and **Supplementary**

Note 2. Taking advantage of the pump CW laser, we also use calibrated Raman thermometry to measure the temperature of the metasurface in-situ during the experiments (comprehensive details are provided in the Methods section).

Figure 2a displays the measured transmission spectra of the metasurface as a function of pump laser intensity (3 μm beam diameter), with the corresponding temperatures ranging from 20°C to 500°C. As the pump intensity increases, the transmission dips associated with MD at around 695 nm and ED at around 800 nm red shift and become less pronounced. Notably, the ED resonance experiences a larger shift (≈ 40 nm) than the MD resonance (≈ 22 nm), which can be attributed to two main reasons. First, the thermo-optical coefficient of a-Si is higher in the spectral region of the ED resonance than at the MD resonance position, leading to a greater refractive index change with temperature near 800 nm. Second, the ED mode exhibits a higher field enhancement and Q-factor than the MD, resulting in stronger light-matter interactions and greater sensitivity to temperature-induced refractive index changes. This enhanced field confinement can induce larger shifts in the ED resonance as the metasurface heats up. When cooling the sample (after exposure to the maximum pump intensity), the transmission spectrum returns to its initial state, indicating that the applied pump intensity can reversibly tune the metasurface’s optical properties without permanent modifications of the materials, such as laser-induced crystallization or oxidation of a-Si[37, 38, 39]. To model the temperature-dependent response of the metasurface, we first extrapolated the a-Si experimental refractive index data beyond 220°C using an approach that we validated against available literature for other materials [29, 40, 41, 42] (see **Supplementary Note 4**). Simulations are in excellent agreement with the experimental data, capturing the trends in transmission modulation with increasing laser intensity **Figure 2b**.

To assess the existence and magnitude of nonlinear variations in the transmitted signal due to thermo-optical effects, particularly near the ED resonance at 800 nm, we analyze the evolution of transmission at selected wavelengths. The pump intensity-dependent transmission at four probe wavelengths (488 nm, 750 nm, 800 nm, and 815 nm) is plotted in **Figure 2c**, clearly showing a nonlinear response of the metasurface at wavelengths around the ED resonance. For the 488 nm probe, which is far from resonance, there is minimal change in transmission, indicating that the thermo-optical effect is less pronounced at this wavelength because of the low thermo-optical coefficient of a-Si and the flat spectrum. In contrast, at 750 nm (left of resonance) and 800 nm (on resonance), there is a significant negative and positive nonlinear change in the transmission as the pump intensity increases, respectively. The nonlinearity is particularly strong at 800 nm, where the ED resonance occurs, leading to a sharp increase in transmission with increasing pump intensity, reaching up to $\approx 470\%$ $\Delta T/T$, (from 0.09 to 0.51) at ≈ 5.6 $\text{mW}/\mu\text{m}^2$ intensity. At 815 nm probe wavelength, we also observe a unique behavior: transmission first decreases from 0.32 to 0.22 (-30% at ≈ 1.5 $\text{mW}/\mu\text{m}^2$) and then increases, reaching the initial value at ≈ 3 $\text{mW}/\mu\text{m}^2$ and then raising up to 0.42 (+30%) for pump a pump intensity of ≈ 5 $\text{mW}/\mu\text{m}^2$, eventually plateauing at higher intensities. Numerical simulations confirm the trends observed in experiments, with significant transmission modulation occurring near the resonant wavelengths (777 nm, 800 nm, and 813 nm). In comparison, the off-resonance wavelength (488 nm) remains largely unaffected (**Fig. 2d**). The good agreement between experimental and simulated results demonstrates the accuracy of the material and electromagnetic models in capturing TONL of the metasurface. Based on the calculations, with improvements in the fabrication, up to $\approx 1360\%$ $\Delta T/T$ (from 0.05 to 0.73) is possible thanks to a gigantic TONL at the resonance wavelength of 800 nm.

TONL in transient optical response To investigate the transient TONL in a-Si metasurface, we performed time-resolved measurements and simulations under various pump and probe conditions as demonstrated schematically in **Figure 3a**. The transient response was measured by probing the metasurface at the resonance wavelength (**Fig. 3**) and near resonance wavelength (**Fig. 4**) while pumping it with the 488 nm continuous wave (CW) laser using different beam sizes and intensity levels. The 488 nm CW pump laser was modulated at 50 kHz, with a transient modulation time of about 2 ns, which is much faster than the heating and cooling times of the metasurface. As such, this modulation does not influence the measured transient dynamics, allowing us to capture the thermo-optical response of the system accurately. The details of the $\Delta T/T$ setup can be found in Methods and **Supplementary Note 2**. The resulting $\Delta T/T$ dynamics provide insight into the interaction between optical heating and the time evolution of the metasurface’s refractive index, highlighting the role of transient TONL in modulating light transmission.

Figure 3b shows the experimentally measured normalised $\Delta T/T$ at 800 nm probe wavelength (i.e. at the ED resonance) for three different pump beam radii (0.75 μm - blue, 1.5 μm - red, and 2.25 μm - yellow) but constant pump intensity of 2.2 $\text{mW}/\mu\text{m}^2$. Transmission is instead probed in a central region with a constant diameter of

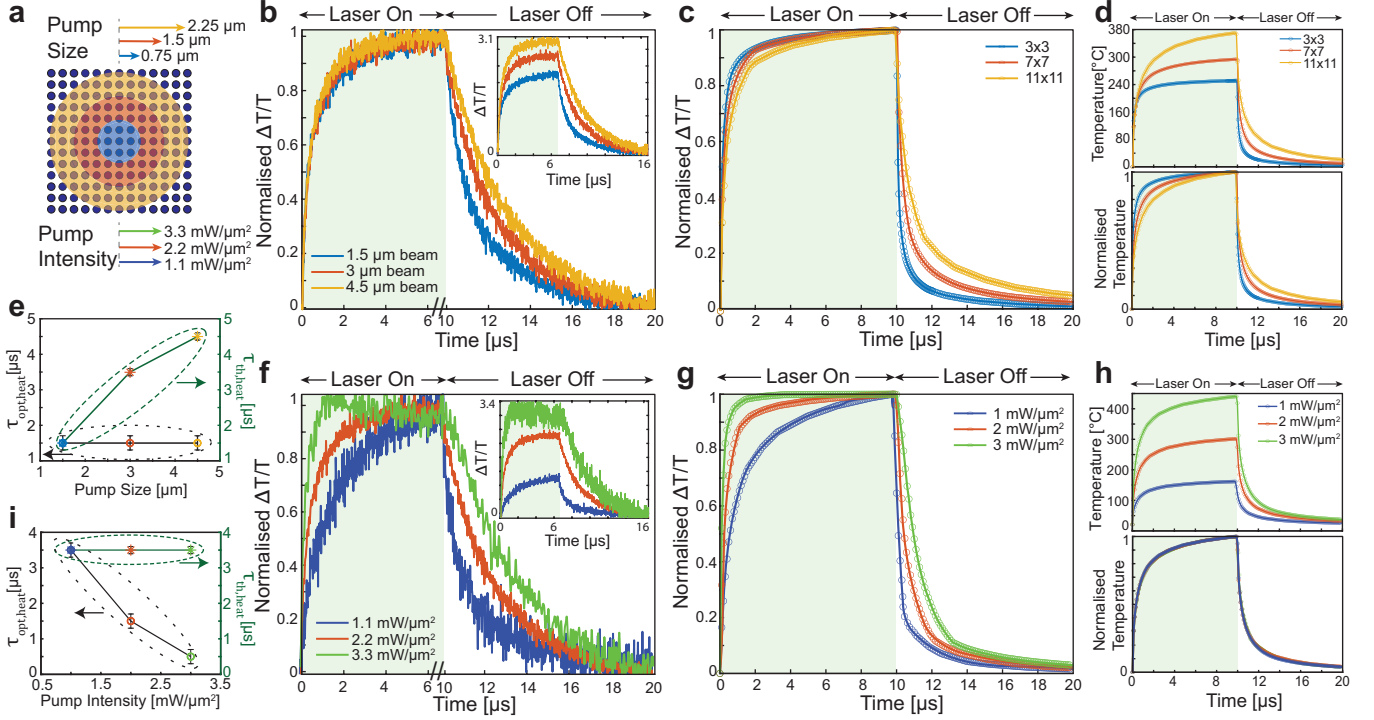


Figure 3: The measured and simulated transient TONL at resonance (800 nm). **a** The schematic illustration of the metasurface with the pump beams of 0.75 (blue), 1.5 (red), and 2.25 (yellow) μm in radius used in panel **b** and the pump intensities of 1.1 (deep blue), 2.2 (red), and 3.3 (green) $\text{mW}/\mu\text{m}^2$ in panel **f** with the radius of 1.5 μm . In all measurements, the probe size was 0.75 μm in radius. **b** The measured normalised $\Delta T/T$ of the metasurface at 800 nm probe for the 1.5 (blue), 3 (red), and 4.5 (yellow) μm 488 nm pump beams in diameter at 2.2 $\text{mW}/\mu\text{m}^2$. The inset shows the nonnormalised transmission, $\Delta T/T$, of the same cases. **c** The simulated normalised $\Delta T/T$ of the 3 by 3 (blue), 7 by 7 (red), and 11 by 11 (yellow) array of nanodisks at 800 nm probe while pumping at 488 nm at 2 $\text{mW}/\mu\text{m}^2$. **d** The simulated transient (upper) and normalised transient (lower) temperatures of the 3 by 3 (blue), 7 by 7 (red), and 11 by 11 (yellow) array of nanodisks at 2 $\text{mW}/\mu\text{m}^2$ pump intensity. **e** The measured $\tau_{opt,heat}$ in **b** and calculated $\tau_{th,heat}$ in **d** versus pump diameter. **f** The measured normalised $\Delta T/T$ of the metasurface at 800 nm probe for 1.1 $\text{mW}/\mu\text{m}^2$ (deep blue), 2.2 $\text{mW}/\mu\text{m}^2$ (red), and 3.3 $\text{mW}/\mu\text{m}^2$ (green) intensity 488 nm 3 μm in diameter pump beams. The inset shows $\Delta T/T$ of the same cases. **g** The simulated normalised $\Delta T/T$ of the 7 by 7 array of nanodisks for the 1 $\text{mW}/\mu\text{m}^2$ (deep blue), 2 $\text{mW}/\mu\text{m}^2$ (red), and 3 $\text{mW}/\mu\text{m}^2$ (green) 488 nm pump intensities at 800 nm probe wavelength. **h** The simulated transient (upper) and normalised transient (lower) temperatures of the 7 by 7 array of nanodisks for the 1 $\text{mW}/\mu\text{m}^2$ (deep blue), 2 $\text{mW}/\mu\text{m}^2$ (red), and 3 $\text{mW}/\mu\text{m}^2$ (green) 488 nm pump intensities. **i** The measured $\tau_{opt,heat}$ in **f** and calculated $\tau_{th,heat}$ in **h** versus pump intensity.

1.5 μm , equivalent to approximately 3 by 3 meta-atoms. Increasing the pump beam diameter while keeping the intensity unchanged in the probed region allows us to assess the impact of collective heating effects [43] on transient TONL. In fact, the constant intensity ensures that light absorption and heat dissipation in each meta-atom (i.e. self-heating) are the same in all measurements. On the other hand, illuminating more meta-atoms (larger beam) results in a larger contribution of heat diffusion (i.e. collective heating) onto the final temperature of the meta-atoms in the central region (details of the configuration is in **Supplementary Note 2**). In agreement with the steady-state results (**Figure 2c**, yellow curve), for all beam sizes $\Delta T/T$ increases during the "Laser On" phase and decreases when the laser is turned off. Notably, while the characteristic time of the optical signal in the "Laser On" phase ($\tau_{opt,heat}$), i.e. during heating, is approximately constant, the characteristic time during the "Laser Off" phase ($\tau_{opt,cool}$), i.e. cooling, depends on the beam size, smaller beams leading to faster changes in transmission.

Additionally, as shown in the inset of **Fig. 3b**, the amplitude of $\Delta T/T$ increases with the beam diameter. These observations depend on the elevated temperatures caused by the increase in collective heating effects with the beam diameter. We also performed COMSOL simulations to model the $\Delta T/T$ response of metasurfaces consisting of 3 by 3, 7 by 7, and 11 by 11 arrays of nanodisks and mimic the effect of increasing beam diameters (**Fig. 3c**) (see Methods for the details of the simulations). These also show that larger arrays (corresponding to larger beams) exhibit slower transient responses due to the more distributed collective heating effects and higher temperatures (**Fig. 3d**). With the model, we also compute the temperature evolution of each system and the associated thermal characteristic time (τ_{th}) for heating and cooling. We obtain $\tau_{th,heat}$ equal to 1.5, 3.5 and 4.5 μs , and $\tau_{th,cool}$ equal to 1.4, 3.2 and 5.6 μs for 3 by 3, 7 by 7, and 11 by 11 array of nanodisks, respectively. Interestingly, while $\tau_{th,heat}$ becomes slower for larger arrays, $\tau_{opt,heat}$ remains approximately constant and equal to $\approx 1.5 \mu s$, as observed in experiments (**Fig. 3e**). The increased temperatures at larger beam diameters, caused by collective heating, amplify thermo-optical nonlinear responses in $\Delta T/T$, enhancing transmission dynamics and decoupling them from thermal dynamics. Small differences between the calculated and measured characteristic times of the transmission modulation can arise from the unaccounted cold nanoresonators around the heated region or a minor mismatch in the thermal parameters of the materials. Overall, these results confirm the critical role of beam size in modulating the transient optical response of the metasurface.

The influence of pump intensity on the transient response is shown in **Figure 3f**, which illustrates the normalised $\Delta T/T$ at low (1.1 $mW/\mu m^2$), medium (2.2 $mW/\mu m^2$), and high (3.3 $mW/\mu m^2$) laser intensity levels. The inset of **Figure 3f** shows $\Delta T/T$, providing insight into the amplitude changes under different intensity conditions. As expected, higher pump intensities (green curve) result in stronger modulation, i.e. a larger change in transmission as a consequence of elevated temperatures (**Fig. 3d**), confirming the strong thermo-optical nonlinear effect in the metasurface.

Contrary to the case of increasing beam size, **Figure 3h** shows that $\tau_{th,heat}$ and $\tau_{th,cool}$ remain constant for different pump intensities, as shown also in previous works [44, 28]. Specifically, they are equal to 3.5 μs and 3.2 μs , respectively. However, in **Figure 3f** we interestingly observe that $\tau_{opt,heat}$, and $\tau_{opt,cool}$ vary significantly with the pump intensity, $\tau_{opt,heat}$ decreasing from $\approx 6 \mu s$ to $\approx 0.5 \mu s$ when the intensity increases from 1.1 $mW/\mu m^2$ to 3.3 $mW/\mu m^2$ (**Fig. 3i**). This apparent discrepancy is a unique consequence of the TONL on $\Delta T/T$. Although the thermal response of the metasurface (heating and cooling rates) remains unaffected by the pump intensity, TONL accelerate the effect on $\Delta T/T$, resulting in a much faster modulation of the signal at higher intensities. We confirmed the experimental result with numerical simulations, achieving excellent agreement regarding transient times and magnitudes (**Fig. 3g**). This further highlights how TONL can decouple the thermal response from the transient optical behavior, creating a situation where optical modulation speeds do not directly correspond to the thermal dynamics of the system.

We finally consider the case where we probe the transient response of the metasurface at a wavelength that is red-shifted compared to the ED resonance mode for which a non-monotonic evolution of the transmission signal with incident intensity was observed in steady-state. Because of experimental limitations (available bandpass filters), we used a metasurface comparable to that presented above but with the ED resonance at 770 nm (nanodisk D of 280 nm, P of 380 nm, and H of 100 nm) and probed it at 785 nm (**Fig. 4a**). **Figure 4b** (upper), shows the normalized $\Delta T/T$ for 1.1 $mW/\mu m^2$ and 3.3 $mW/\mu m^2$ pump intensities. A markedly different response from that observed on-resonance (**Fig. 3f**) is obtained. Most strikingly, there exist clear variations in both the characteristic times and the shape of $\Delta T/T$ with pump intensity, highlighting the profound influence of TONL on the transient response. At 1.1 $mW/\mu m^2$ transmission monotonically decreases. Indeed upon photothermal heating the resonance redshifts (≈ 12 nm), eventually matching the probe wavelength, which thus reaches the minimum transmission value. Once the laser is turned off, the resonance shifts back to its initial position resulting in a monotonic increase in the transmission. At 3.3 $mW/\mu m^2$, however, as time passes and temperature increases further, the resonance redshifts beyond the probe wavelength, reaching ≈ 30 nm shift at steady-state. When the resonance center becomes more red-shifted than the probe wavelength, transmission increases again. We thus observe that when the laser is turned on, transmission shows an extremely fast dip (≈ 300 ns), followed by rapid recovery to the initial transmission value (i.e. zero differential transmission). When the laser is turned off, the system similarly exhibits a fast dip in transmission and a quick recovery. This trend can be better understood by considering **Figure 4d**, acquired in steady state. During a dynamic modulation with the 488 nm CW laser, the transmission signal evolves in time along the green curve, up to 1.1 $mW/\mu m^2$ or 3.3 $mW/\mu m^2$ pump intensities, as shown by the blue and yellow arrows, with non-uniform speed due to the non-linear change in temperature.

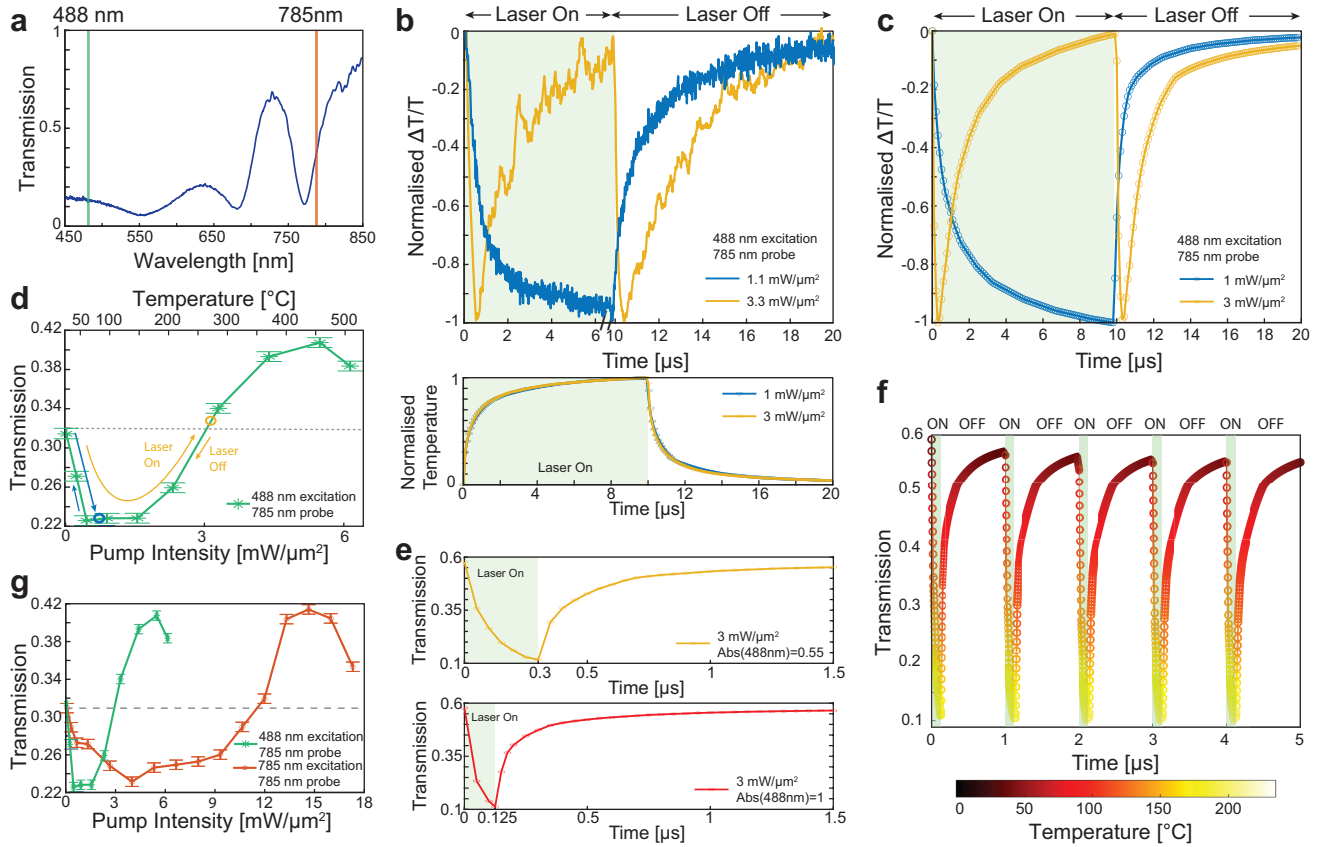


Figure 4: The measured and simulated transient TONL at near resonance probing. **a** The transmission spectrum of the metasurface with ED resonance at 770 nm and the spectral positions of the pump (green) and probe (orange) wavelengths of 488 nm and 785 nm, respectively. **b** The measured normalised $\Delta T/T$ (upper) and normalised temperature (lower) of the metasurface, for the 1.1 $\text{mW}/\mu\text{m}^2$ (blue), and 3.3 $\text{mW}/\mu\text{m}^2$ (yellow) 488 nm pump intensities at 785 nm probe wavelength. **c** The simulated normalised $\Delta T/T$ of the 7 by 7 array of nanodisks for the 1 $\text{mW}/\mu\text{m}^2$ (blue), and 3 $\text{mW}/\mu\text{m}^2$ (yellow) 488 nm pump intensities at 785 nm probe wavelength. **d** The measured pump intensity-dependent transmission of the metasurface at the pump and probe wavelengths of 488 and 785 nm, respectively. Upper x-axis shows the measured temperatures corresponding to the pump intensities. The blue (yellow) arrow illustrates the gradual change in transmission at 1.1 (3.3) $\text{mW}/\mu\text{m}^2$ in **b**. **e** The simulated $\Delta T/T$ at 785 nm (upper) for the laser is turned off at 300 ns at 3 $\text{mW}/\mu\text{m}^2$ pump intensity with 0.55 absorption at 488 nm and (lower) for the laser is turned off at 125 ns at 3 $\text{mW}/\mu\text{m}^2$ pump intensity with unity absorption at 488 nm. **f** The simulated transient transmission at 785 nm for the modulated 488 nm laser at 1 MHz with laser-on time equals 125 ns at 3 $\text{mW}/\mu\text{m}^2$ intensity with unity absorption at 488 nm. **g** The measured pump intensity-dependent transmission of the metasurface at the probe wavelength of 785 nm for the pump wavelengths of 488 nm (blue) and 785 nm (orange).

For 3.3 $\text{mW}/\mu\text{m}^2$ pump intensity, the final transmission has the same amplitude as the initial one, as observed by the recovery of $\Delta T/T$ in **Figure 4d**, yellow curve. Overall, in this particular condition we observe that while the laser is modulated at 50 kHz , the transmission signal is effectively modulated at twice this speed, i.e. 100 kHz . We emphasize that this complex optical behavior is not mirrored by the thermal response, as **Figure 4b** (lower) shows that the temperature monotonically increases when the laser is on and decreases after it is turned off. This discrepancy between the optical and thermal responses confirms that the system is no longer linear and is governed by highly complex nonlinearities that effectively decouple the transient optical response from the underlying thermal dynamics. In **Figure 4c**, we present simulated normalized $\Delta T/T$ for a 7 by 7 nanodisk array, resonant at 770 nm, probed at 785 nm as in the experimental conditions. The simulations closely replicate

the measured behavior, confirming that the transient optical modulation is governed by both the intensity of the pump laser and the resonant properties of the metasurface. Overall, TONL introduces a decoupling of thermal and optical dynamics and the resonant nature of the metasurface introduces non-monotonic evolutions of the optical signal with temperatures. Together, they generate unique and non-intuitive behaviors in the metasurface transient optical properties, further reinforcing the importance of TONL in driving advanced optical modulation effects.

To explore the limits of modulation speed in the studied system, we now concentrate on controlling independently the laser-on and laser-off phases. Indeed, although above we demonstrated an effective doubling of the modulation speed, we observe that the transmission recovery time during the laser-off phase increases with increasing incident power. The upper panel in **Figure 4e** shows the calculated transient transmission when the laser is turned off after 300 ns, instead of 10 μ s, for a pump intensity of 3 mW/ μ m². The initial sharp drop in transmission (from 0.6 to 0.1 corresponds to \approx 85% change in T) follows the behavior reported in **Figure 4b-c** for the high pump intensity case (yellow curve, laser on phase). However, when the laser is turned off, the cooling dynamic follows the evolution observed for the low pump intensity case (blue curve, laser off phase). This is due to the fact that the cooling process is governed solely by the temperature reached at 300 ns, irrespective of the illumination intensity used. The temperature at the minimum of $\Delta T/T$ is the same for the high and low pump intensity cases, as it corresponds to the shift of the ED resonance to the probe wavelength. However, the heating rate and thus the time it takes to reach this temperature strongly depends on the used intensity. This behavior effectively decouples the heating and cooling rates, enabling faster modulation. The modulation speed, therefore, becomes even faster than what would be expected from traditional thermo-optical switches [21, 45]. Finally, we also consider the case in which absorption of the metasurface at 488 nm is unity instead of 0.55 as in our experiments (**Fig. 4e** lower panel). As just discussed, a higher heating rate further accelerates the optical modulation rate resulting in the minimum transmission occurring at just 125 ns. Moreover, thanks to flash heating, the heated area is more localized resulting in faster cooling and recovery of the transmission when the laser is turned off compared to the case of absorption is equal to 0.55. This unique behavior opens the possibility for operating the metasurface in the MHz range with very high modulation depths (**Fig. 4f**), making it significantly more efficient than conventional thermo-optical switches, which are typically constrained by slower thermal response times. By leveraging this fast modulation mechanism, we demonstrate that TONL in a-Si metasurfaces has the potential to break the typical limitations of thermal-based modulation, offering much faster switching capabilities.

Comparison between the dual and single band operations When using the 488 nm laser for photothermally heating the metasurface (**Figure 4a**, green line), the pump wavelength is spectrally far from any resonance, corresponding to dual-band operation. Consequently, absorption at the pump wavelength remains essentially constant with temperature and, as the pump intensity increases, the steady-state temperature of the metasurface increases as well (**Fig. 4d**). Therefore, the observed steady-state and dynamic transmission changes are purely due to TONL at the probe wavelength. In contrast, when using a 785 nm pump laser (**Figure 4a**, orange line), close to the ED resonance of the metasurface, the system operates in a single-band mode, where both thermo-optical and photo-thermal nonlinearities must be considered [46, 47, 48, 16]. As shown in **Figure 4g**, orange curve, at low pump intensities, transmission decreases as the metasurface heats up but not as much as with 488 nm pumping (green curve) because of the much lower absorption at 785 nm. As the pump intensity increases, the photo-thermal nonlinearity becomes more pronounced, resulting in an enhanced nonlinear response (see **Supplementary Fig. 6**). Eventually, the evolution of the transmission with pump intensity follows the same shape as with 488 nm excitation but with a non-linear stretching of the x-axis due to the non-linear change in absorbed power. The interaction between the heating effects and the resonance properties of the metasurface thus causes the transmission to behave in a more complex manner compared to the dual-band operation.

3 Discussion

Our study reveals novel insights into the transient and steady-state TONL in a-Si metasurfaces, building on existing literature primarily focused on steady-state nonlinear optical effects. The results highlight the unique ability of a-Si metasurfaces to exhibit nonlinear and non-monotonic transmission changes and to decouple the transient optical response from the slower thermal dynamics of the system. These two effects, driven by TONL, eventually enable high-speed transmission modulation while benefiting from the resonant nature of the system to achieve large modulation amplitudes.

The role of collective heating was also explored in our experiments, particularly by varying the pump beam size

and intensity. We found that smaller beams induce faster thermal responses due to more localized heating, while larger beams result in slower responses due to the increase of collective heating effects. This behavior is consistent with the predictions of earlier work [49], where the spatial distribution of heat plays a significant role in determining the overall optical response of the metasurface. More importantly, the enhanced collective heating effects from larger beams result in higher temperatures, leading to stronger TONL. Consequently, while the thermal response time increases with the size of the irradiated system, the optical response time remains nearly unchanged, allowing for faster modulation times than anticipated. Furthermore, we showed that increasing the pump beam intensity, for a given beam size, can dramatically reduce the optical response characteristic time, while leaving the thermal response characteristic time unaltered. This provides a simple and direct way to control the dynamics of the optical response of the metasurface.

Finally, we briefly discuss the use of Raman thermometry for in-situ temperature measurements. Raman thermometry is indeed a highly effective method for measuring the temperature of silicon materials [50, 51]. Monocrystalline silicon (c-Si) displays a pronounced and distinct Raman peak, which arises from the interaction of light with phonon modes. The temperature of Si nanoparticles can thus be determined based on the linewidth broadening of the Raman peak or its spectral shift as well as from the reduction in the anti-Stokes/Stokes signal ratio [52, 53]. However, it has been observed that Mie resonances, present in both metals and semiconductors, can have a significant impact on the Raman scattering spectrum. Specifically, they can affect the linewidth of the spectral peaks as well as alter the anti-Stokes/Stokes ratio, with the latter being influenced by the Purcell effect [54, 55]. To mitigate the impact of Mie resonances, we employed a 488 nm pump laser to induce the Raman signal, as the spectrum of the metasurface at this wavelength lacks Mie-like resonances and remains almost flat. Due to the broadened and more chaotic Raman signal in amorphous materials, there have been fewer attempts in the literature to apply Raman thermometry to amorphous silicon [56, 57]. In our approach, we decompose the Raman peaks to isolate the intensity and central positions of each vibrational mode of a-Si. This reveals several vibrational peaks, including a distinct transverse optical phonon mode at 470 cm^{-1} (see **Supplementary Note 3**). As we showed through the excellent agreement of experiments and simulations, the anti-Stokes/Stokes ratio of this mode can be used to reliably measure the local a-Si temperature during the experiments.

Overall, high-speed all-optical photonic devices are attracting growing interest and our findings provide new guidelines on how to exploit TONL towards rapid modulation. The ability of a-Si metasurfaces to decouple the transient optical response from thermal dynamics presents a new avenue for developing fast, tunable optical modulators, switches, and sensors. To further enhance the transient nonlinearities and modulation rates, one can think of modulating higher Q factor resonances such as q-BIC [27] or surface lattice resonances (SLR) [58], as well as pumping the system at wavelengths with near-unity absorption [59, 60] or utilizing the concept of thermo-optical bistability [26, 27]. Furthermore, by exploiting nonlinear changes in the absorption rate of the pump beam, the modulation rates can be further enhanced, and complex dynamic responses can be engineered. Moreover, the excellent agreement between our experimental results and COMSOL simulations reinforces the robustness of the TONL mechanism in a-Si metasurfaces, further supporting their potential for high-performance applications in telecommunications and optical computing.

In conclusion, this study provides a comprehensive exploration of both steady-state and transient TONL in a-Si metasurfaces. The novel decoupling of optical and thermal responses opens up new possibilities for achieving ultrafast optical modulation, surpassing the limitations imposed by thermal dynamics in traditional metasurface systems. This work represents a significant step forward in understanding and harnessing TONL for advanced photonic applications.

4 Methods

Sample preparation. The metasurface samples were fabricated on a $550\text{ }\mu\text{m}$ thick fused silica substrate. A 100 nm thick layer of amorphous silicon (a-Si) was deposited onto the substrate using plasma-enhanced chemical vapor deposition (PECVD) at 550°C . This deposition technique ensures a uniform a-Si layer with well-controlled thickness, which is critical for the metasurface’s optical performance. Electron beam lithography (EBL-Raith EBPG5000+) was employed to pattern the a-Si nanodisks. A 120 nm thick ZEP 520A resist was spin-coated onto the a-Si layer and subsequently patterned using EBL (100 kV and $200\text{ }\mu\text{C}/\text{cm}^2$ beam) to define the nanodisk structures. After developing the resist, the patterned ZEP resist served as a mask for the etching process. The a-Si nanodisks were then etched into the substrate using argon ion beam etching (Veeco Nexus IBE350) (170V

and 175mA beam). The back surface of the chips was also etched by IBE to remove the deposited a-Si at the back surface of the chips. After the etching process, the remaining ZEP resist was removed by soaking the samples in acetone. To ensure the complete removal of any residual organic material, the samples were subjected to a final low-power microwave plasma cleaning (Tepla-300) (500W and 400ml/min O₂), which further cleaned the surface without affecting the nanodisk structures.

Setups. *Steady-state measurements (Fig.1b, Fig.2, and Fig.4d):* The experimental setup used for spectral, Raman, and $\Delta T/T$ measurements is a custom-built system designed to enable precise control and visualization of the metasurface sample. The setup includes a microscopy section to visually inspect the sample, which utilizes a high numerical aperture (NA 0.8) 100x objective (Nikon-LU Plan ELWD) and a CMOS camera (Thorlabs- CS165MU). The halogen lamp (OSL2IR-Thorlabs) is used for the transmission measurements. The system is coupled with an Andor Shamrock 750 spectrometer body equipped with an iDus 420 CCD camera for spectral measurements. The system is equipped with a 488 nm OBIS LX laser, which can be digitally modulated up to 150 MHz. This laser serves as the primary pump source for many of the experiments, including Raman and $\Delta T/T$ measurements. Additionally, a 785 nm laser is integrated into the setup for non-degenerate (single-band) measurements, allowing us to explore the metasurface’s behavior under different excitation wavelengths. For Raman and steady-state transmission measurements, the 488 nm pump laser is filtered using a series of cut-off filters to remove any unwanted pump light. The spectrometer is configured with a high line number grating to increase the spectral resolution, ensuring that even subtle shifts in the Raman spectra are captured with high precision. It is worth noting that $\Delta T/T$ is defined as $(T(\lambda, intensity) - T_0(\lambda))/T_0(\lambda)$ where $T_0(\lambda)$ is the unperturbed room temperature transmission.

Transient measurements (Fig.3 and Fig.4a): $\Delta T/T$ measurements are conducted using a commercial time-correlated single photon counting (TCSPC) system (PicoQuant Hydrharp 400) coupled with a silicon single-photon avalanche diode (Si SPAD- Micro Photon Devices PDM Series) detector, providing a time resolution of approximately 20 ps. (NA 0.8) 100x objective is used in these measurements. In these measurements, the 488 nm laser was modulated at 50 kHz using a square wave trigger signal (% 50 duty cycle) (TTi TG320), which serves as a synchronization signal for the TCSPC module. To selectively probe specific spectral regions of transmitted white light, narrow bandwidth (≈ 3 nm in FWHM) bandpass filters were employed, isolating the wavelengths of interest for detailed analysis. It is worth noting that $\Delta T/T$ is defined as $(T(\lambda, time) - T_0(\lambda))/T_0(\lambda)$.

COMSOL modelling of the TONL. All simulations were performed by using the Finite Element Method (FEM) based commercial software COMSOL Multiphysics (COMSOL Multiphysics 6.2).

Transient photo-thermal heating simulations (Fig.3d and Fig.3e): The simulated structures were modeled in close agreement with the experimental geometric parameters (H=100 nm, D=290 nm, and P=380 nm). A 3D model was built with 3 by 3, 7 by 7, and 11 by 11 arrays of a-Si nanopillars supported on SiO₂ to mimic the area irradiated with the pump laser beam as we changed the beam diameter from 1 to 3 μm . Each structure was placed in a 400 nm thick air layer of refractive index 1, lying on the surface of a 400 nm thick SiO₂ background medium layer, with both dimensions along the vertical direction. The lateral dimensions of the simulated domain were varied with the size of the array simulated. The simulation domain was truncated by exploiting 300 nm thick Infinite Element Domains (IEDs) in all of the spatial directions. The nanopillar’s optical properties were described by using the temperature-dependent refractive indices we measured by ellipsometry. A monochromatic plane wave at normal incidence from above was utilized to excite the metasurface. The wavelength of the input light was set to the wavelength corresponding to the pump laser. Laser power was varied in the simulations to match the experimental conditions. The laser illumination was switched on for 10 μs and subsequently switched off to study the heating and cooling dynamics of the illuminated metasurface region. Maxwell’s equations were then solved in the transient frequency domain for the total field at the excitation wavelength. The resistive losses could then be evaluated from the model through the volume integral in the subdomain of concern. With the resistive losses calculated from electromagnetic simulation, the resultant temperature dynamics were simulated with a 3D heat transfer model. The nanoparticle array and SiO₂ substrate were set as heat sources, with heat dissipated according to the integration of resistive losses. The ambient temperature was set at 20°C and the average temperatures of the simulated particles are considered in the study. We also considered the influence of temperature increase on the heat conductivity and electric permittivity of the materials.

Metasurface unit cell simulations at elevated temperatures (Fig.2b): The metasurface unit cell simulation (Electromagnetic Waves, Frequency Domain) at different temperatures was done by using the measured n and k dataset at different temperatures. Due to the limitation of ellipsometry, we extrapolated the n and k at higher

than 220⁰C (see **Supplementary Note 4**).

We also mapped the transient temperatures to the perturbed transmission using the abovementioned simulations and obtained $\Delta T/T$ simulations for the specific cases in the study.

Raman thermometry. We employed Raman spectroscopy to measure the local temperature of the metasurface, adapting a method previously used for c-Si [16, 52, 61, 25] to a-Si. Unlike c-Si, a-Si exhibits a more complex and broadened Raman spectrum due to the amorphous nature of its phonon modes. The most pronounced phonon mode in a-Si appears at approximately 470 cm⁻¹, corresponding to the transverse optical (TO) phonon mode. To determine the local temperature of the metasurface, we fitted Gaussian functions to the measured Raman spectrum to accurately identify the center and amplitude of the 470 cm⁻¹ TO mode. The amplitude of this mode was then used to calculate the temperature. Specifically, we applied the same temperature calculation model that utilizes the intensity ratio of the Stokes and anti-Stokes Raman peaks. The equation used is:

$$\frac{I_A}{I_S} = \exp\left(\frac{-\hbar\omega_p}{k_B T}\right) \quad (1)$$

where I_A and I_S are the intensities of Anti-Stokes and Stokes Raman signals, respectively, k_B is the Boltzmann constant, \hbar is the Planck constant, ω_p is the frequency of the phonon mode, and T is the temperature.

Data Availability Statement

All the data supporting the findings of this study are presented in the Results section and Supplementary Information are available from the corresponding authors upon reasonable request.

Acknowledgements

G.N.N. and G.T. acknowledge the support of the Swiss National Science Foundation (Starting Grant 211695). END and GT acknowledge the support of the Swiss National Science Foundation (Eccellenza Grant 194181) and the STI Discovery Grant (EPFL). ARB acknowledges the support of SNSF Eccellenza Grant 194181 and SNSF Swiss Postdoctoral Fellowship TMPFP2_217040. The authors also acknowledge the support of the Center of MicroNanoTechnology (CMi) at EPFL.

Author contributions

G.T. supervised all aspects of the project. O.C.K. prepared the sample and performed the experiments and simulations. G.N.N. built the transient simulation model. A.R.B. and E.N.D. played an active role in the discussions and building the setup. G.T. and O.C.K. wrote the paper, with input from all the other authors.

Competing interests

The Authors declare no competing interests.

Figure Captions

Optical properties of the proposed a-Si metasurface. **a** The schematic illustration of a-Si metasurface on Fused Silica substrate (P, D, and H denote the periodicity, diameter, and height of the disks, respectively). **b** The schematic illustration of the modulated CW laser signal(upper), the temperature evolution in time(middle) and differential transient transmission(lower), $\Delta T/T$, of the metasurface. **c** The transmission spectra of the fabricated (blue) and simulated (orange) metasurfaces. The inset shows the SEM image of the fabricated metasurface with P of 380 nm, D of 290 nm, and H of 100 nm. **d** The measured real part, n , and imaginary part, k , of the refractive indices of a-Si at 20 °C, 70 °C, 120 °C, 170 °C, and 220 °C.

The measured and simulated TONL in steady-state. **a** The measured transmission spectra of the metasurface under different pump intensities. The legend specifies the temperatures measured by Raman thermometry at the corresponding pump intensities. The semi-transparent regions specify the probe wavelengths in **c**. **b** The simulated transmission spectra of the metasurface under different pump intensities. The semi-transparent regions specify the probe wavelengths in **d**. **c** The measured pump intensity-dependent transmission of the metasurface at the probe wavelengths of 488 nm (blue), 750 nm (orange), 800 nm (yellow), and 815 nm (violet). Upper x-axis shows the measured temperatures corresponding to the pump intensities. **d** The simulated pump intensity (temperature)-dependent transmission of the metasurface at the probe wavelengths of 488 nm (blue), 777 nm (orange), 800 nm (yellow), and 813 nm (violet).

The measured and simulated transient TONL at resonance (800 nm). **a** The schematic illustration of the metasurface with the pump beams of 0.75 (blue), 1.5 (red), and 2.25 (yellow) μm in radius used in panel **b** and the pump intensities of 1.1 (deep blue), 2.2 (red), and 3.3 (green) $\text{mW}/\mu\text{m}^2$ in panel **f** with the radius of 1.5 μm . In all measurements, the probe size was 0.75 μm in radius. **b** The measured normalised $\Delta T/T$ of the metasurface at 800 nm probe for the 1.5 (blue), 3 (red), and 4.5 (yellow) μm 488 nm pump beams in diameter at 2.2 $\text{mW}/\mu\text{m}^2$. The inset shows the nonnormalised transmission, $\Delta T/T$, of the same cases. **c** The simulated normalised $\Delta T/T$ of the 3 by 3 (blue), 7 by 7 (red), and 11 by 11 (yellow) array of nanodisks at 800 nm probe while pumping at 488 nm at 2 $\text{mW}/\mu\text{m}^2$. **d** The simulated transient (upper) and normalised transient (lower) temperatures of the 3 by 3 (blue), 7 by 7 (red), and 11 by 11 (yellow) array of nanodisks at 2 $\text{mW}/\mu\text{m}^2$ pump intensity. **e** The measured $\tau_{opt,heat}$ in **b** and calculated $\tau_{th,heat}$ in **d** versus pump diameter. **f** The measured normalised $\Delta T/T$ of the metasurface at 800 nm probe for 1.1 $\text{mW}/\mu\text{m}^2$ (deep blue), 2.2 $\text{mW}/\mu\text{m}^2$ (red), and 3.3 $\text{mW}/\mu\text{m}^2$ (green) intensity 488 nm 3 μm in diameter pump beams. The inset shows $\Delta T/T$ of the same cases. **g** The simulated normalised $\Delta T/T$ of the 7 by 7 array of nanodisks for the 1 $\text{mW}/\mu\text{m}^2$ (deep blue), 2 $\text{mW}/\mu\text{m}^2$ (red), and 3 $\text{mW}/\mu\text{m}^2$ (green) 488 nm pump intensities at 800 nm probe wavelength. **h** The simulated transient (upper) and normalised transient (lower) temperatures of the 7 by 7 array of nanodisks for the 1 $\text{mW}/\mu\text{m}^2$ (deep blue), 2 $\text{mW}/\mu\text{m}^2$ (red), and 3 $\text{mW}/\mu\text{m}^2$ (green) 488 nm pump intensities. **i** The measured $\tau_{opt,heat}$ in **f** and calculated $\tau_{th,heat}$ in **h** versus pump intensity.

The measured and simulated transient TONL at near resonance probing. **a** The transmission spectrum of the metasurface with ED resonance at 770 nm and the spectral positions of the pump (green) and probe (orange) wavelengths of 488 nm and 785 nm, respectively. **b** The measured normalised $\Delta T/T$ (upper) and nonnormalised temperature (lower) of the metasurface, for the 1.1 $\text{mW}/\mu\text{m}^2$ (blue), and 3.3 $\text{mW}/\mu\text{m}^2$ (yellow) 488 nm pump intensities at 785 nm probe wavelength. **c** The simulated normalised $\Delta T/T$ of the 7 by 7 array of nanodisks for the 1 $\text{mW}/\mu\text{m}^2$ (blue), and 3 $\text{mW}/\mu\text{m}^2$ (yellow) 488 nm pump intensities at 785 nm probe wavelength. **d** The measured pump intensity-dependent transmission of the metasurface at the pump and probe wavelengths of 488 and 785 nm, respectively. Upper x-axis shows the measured temperatures corresponding to the pump intensities. The blue (yellow) arrow illustrates the gradual change in transmission at 1.1 (3.3) $\text{mW}/\mu\text{m}^2$ in **b**. **e** The simulated $\Delta T/T$ at 785 nm (upper) for the laser is turned off at 300 ns at 3 $\text{mW}/\mu\text{m}^2$ pump intensity with 0.55 absorption at 488 nm and (lower) for the laser is turned off at 125 ns at 3 $\text{mW}/\mu\text{m}^2$ pump intensity with unity absorption at 488 nm. **f** The simulated transient transmission at 785 nm for the modulated 488nm laser at 1 MHz with laser-on time equals 125 ns at 3 $\text{mW}/\mu\text{m}^2$ intensity with unity absorption at 488 nm. **g** The measured pump intensity-dependent transmission of the metasurface at the probe wavelength of 785 nm for the pump wavelengths of 488 nm (blue) and 785 nm (orange).

References

- [1] Tian Gu, Hyun Jung Kim, Clara Rivero-Baleine, and Juejun Hu. Reconfigurable metasurfaces towards commercial success. *Nature Photonics*, 17(1):48–58, January 2023. Publisher: Nature Publishing Group.
- [2] Mikhail Y. Shalaginov, Sawyer D. Campbell, Sensong An, Yifei Zhang, Carlos Ríos, Eric B. Whiting, Yuhao Wu, Lei Kang, Bowen Zheng, Clayton Fowler, Hualiang Zhang, Douglas H. Werner, Juejun Hu, and Tian Gu. Design for quality: reconfigurable flat optics based on active metasurfaces. *Nanophotonics*, 9(11):3505–3534, August 2020.
- [3] D. Barton, M. Lawrence, and J. Dionne. Wavefront shaping and modulation with resonant electro-optic phase gradient metasurfaces. *Applied Physics Letters*, 118(7):071104, February 2021.
- [4] Aaron L. Holsteen, Ahmet Fatih Cihan, and Mark L. Brongersma. Temporal color mixing and dynamic beam shaping with silicon metasurfaces. *Science*, 365(6450):257–260, July 2019.
- [5] Zhanni Wu, Younes Ra’di, and Anthony Grbic. Tunable Metasurfaces: A Polarization Rotator Design. *Physical Review X*, 9(1):011036, February 2019.
- [6] M. Zhang, W. Zhang, A. Q. Liu, F. C. Li, and C. F. Lan. Tunable Polarization Conversion and Rotation based on a Reconfigurable Metasurface. *Scientific Reports*, 7(1):12068, September 2017.
- [7] Heng Wang, Zixian Hu, Junhong Deng, Xuecai Zhang, Jiafei Chen, Kingfai Li, and Guixin Li. All-optical ultrafast polarization switching with nonlinear plasmonic metasurfaces. *Science AdvAnceS*, 2024.
- [8] Haejun Chung and Owen D. Miller. Tunable Metasurface Inverse Design for 80% Switching Efficiencies and 144° Angular Deflection. *ACS Photonics*, 7(8):2236–2243, August 2020. Publisher: American Chemical Society.
- [9] Pin Chieh Wu, Ragip A. Pala, Ghazaleh Kafaie Shirmanesh, Wen-Hui Cheng, Ruzan Sokhoyan, Meir Grajower, Muhammad Z. Alam, Duhyun Lee, and Harry A. Atwater. Dynamic beam steering with all-dielectric electro-optic III–V multiple-quantum-well metasurfaces. *Nature Communications*, 10(1):3654, August 2019. Publisher: Nature Publishing Group.
- [10] Helena Weigand, Viola V. Vogler-Neuling, Marc Reig Escalé, David Pohl, Felix U. Richter, Artemios Karvounis, Flavia Timpu, and Rachel Grange. Enhanced Electro-Optic Modulation in Resonant Metasurfaces of Lithium Niobate. *ACS Photonics*, 8(10):3004–3009, October 2021. Publisher: American Chemical Society.
- [11] Maxim R. Shcherbakov, Sheng Liu, Varvara V. Zubyuk, Aleksandr Vaskin, Polina P. Vabishchevich, Gordon Keeler, Thomas Pertsch, Tatyana V. Dolgova, Isabelle Staude, Igal Brener, and Andrey A. Fedyanin. Ultrafast all-optical tuning of direct-gap semiconductor metasurfaces. *Nature Communications*, 8(1):17, May 2017. Publisher: Nature Publishing Group.
- [12] Yu Zhu, Xiaoyong Hu, Hong Yang, and Qihuang Gong. Ultralow-power all-optical tunable double plasmon-induced transparencies in nonlinear metamaterials. *Applied Physics Letters*, 104(21):211108, May 2014.
- [13] Can O. Karaman, Anton Yu Bykov, Fatemeh Kiani, Giulia Tagliabue, and Anatoly V. Zayats. Ultrafast hot-carrier dynamics in ultrathin monocrystalline gold. *Nature Communications*, 15(1):703, January 2024. Publisher: Nature Publishing Group.
- [14] Fatemeh Kiani, Alan R. Bowman, Milad Sabzehparvar, Can O. Karaman, Ravishankar Sundararaman, and Giulia Tagliabue. Transport and Interfacial Injection of d-Band Hot Holes Control Plasmonic Chemistry. *ACS Energy Letters*, 8(10):4242–4250, October 2023.
- [15] Jianqiang Gu, Ranjan Singh, Xiaojun Liu, Xueqian Zhang, Yingfang Ma, Shuang Zhang, Stefan A. Maier, Zhen Tian, Abul K. Azad, Hou-Tong Chen, Antoinette J. Taylor, Jianguang Han, and Weili Zhang. Active control of electromagnetically induced transparency analogue in terahertz metamaterials. *Nature Communications*, 3(1):1151, October 2012. Publisher: Nature Publishing Group.

- [16] Yi-Shiou Duh, Yusuke Nagasaki, Yu-Lung Tang, Pang-Han Wu, Hao-Yu Cheng, Te-Hsin Yen, Hou-Xian Ding, Kentaro Nishida, Ikuto Hotta, Jhen-Hong Yang, Yu-Ping Lo, Kuo-Ping Chen, Katsumasa Fujita, Chih-Wei Chang, Kung-Hsuan Lin, Junichi Takahara, and Shi-Wei Chu. Giant photothermal nonlinearity in a single silicon nanostructure. *Nature Communications*, 11(1):4101, August 2020.
- [17] George P. Zograf, Mihail I. Petrov, Sergey V. Makarov, and Yuri S. Kivshar. All-dielectric thermonanophotonics. *Advances in Optics and Photonics*, 13(3):643–702, September 2021. Publisher: Optica Publishing Group.
- [18] Chien-Hsuan Li, Yu-Lung Tang, Junichi Takahara, and Shi-Wei Chu. Nonlinear heating and scattering in a single crystalline silicon nanostructure. *The Journal of Chemical Physics*, 155(20):204202, November 2021.
- [19] Yuanmu Yang, Wenyi Wang, Abdelaziz Boulesbaa, Ivan I. Kravchenko, Dayrl P. Briggs, Alexander Poretzky, David Geohegan, and Jason Valentine. Nonlinear Fano-Resonant Dielectric Metasurfaces. *Nano Letters*, 15(11):7388–7393, November 2015.
- [20] Khosro Zangeneh Kamali, Lei Xu, Jonathan Ward, Kai Wang, Guixin Li, Andrey E. Miroshnichenko, Dragomir Neshev, and Mohsen Rahmani. Reversible Image Contrast Manipulation with Thermally Tunable Dielectric Metasurfaces. *Small*, 15(15):1805142, 2019. _eprint: <https://onlinelibrary.wiley.com/doi/pdf/10.1002/sml.201805142>.
- [21] Yu Horie, Amir Arbabi, Ehsan Arbabi, Seyedeh Mahsa Kamali, and Andrei Faraon. High-Speed, Phase-Dominant Spatial Light Modulation with Silicon-Based Active Resonant Antennas. *ACS Photonics*, 5(5):1711–1717, May 2018. Publisher: American Chemical Society.
- [22] Seong-Hwan Kim, Jong-Bum You, Yun-Gi Ha, Geumbong Kang, Dae-Seong Lee, Hyeonho Yoon, Dong-Eun Yoo, Dong-Wook Lee, Kyoungsik Yu, Chan-Hyun Youn, and Hyo-Hoon Park. Thermo-optic control of the longitudinal radiation angle in a silicon-based optical phased array. *Optics Letters*, 44(2):411, January 2019.
- [23] William S. Rabinovich, Peter G. Goetz, Marcel W. Pruessner, Rita Mahon, Mike S. Ferraro, Doe Park, Erin F. Fleet, and Michael J. DePrenger. Two-dimensional beam steering using a thermo-optic silicon photonic optical phased array. *Optical Engineering*, 55(11):111603, August 2016. Publisher: SPIE.
- [24] Ying Che, Tianyue Zhang, Tan Shi, Zi-Lan Deng, Yaoyu Cao, Bai-Ou Guan, and Xiangping Li. Ultrasensitive Photothermal Switching with Resonant Silicon Metasurfaces at Visible Bands. *Nano Letters*, 24(2):576–583, January 2024. Publisher: American Chemical Society.
- [25] Tianyue Zhang, Ying Che, Kai Chen, Jian Xu, Yi Xu, Te Wen, Guowei Lu, Xiaowei Liu, Bin Wang, Xiaoxuan Xu, Yi-Shiou Duh, Yu-Lung Tang, Jing Han, Yaoyu Cao, Bai-Ou Guan, Shi-Wei Chu, and Xiangping Li. Anapole mediated giant photothermal nonlinearity in nanostructured silicon. *Nature Communications*, 11(1):3027, June 2020.
- [26] Michele Cotrufo, Andrea Cordaro, Dimitrios L. Sounas, Albert Polman, and Andrea Alù. Passive bias-free non-reciprocal metasurfaces based on thermally nonlinear quasi-bound states in the continuum. *Nature Photonics*, 18(1):81–90, January 2024. Publisher: Nature Publishing Group.
- [27] Alexander Barulin, Olesia Pashina, Daniil Riabov, Olga Sergaeva, Zarina Sadrieva, Alexey Shcherbakov, Viktoriia Rutckaia, Jörg Schilling, Andrey Bogdanov, Ivan Sinev, Alexander Chernov, and Mihail Petrov. Thermo-Optical Bistability Enabled by Bound States in The Continuum in Silicon Metasurfaces. *Laser & Photonics Reviews*, n/a(n/a):2301399. _eprint: <https://onlinelibrary.wiley.com/doi/pdf/10.1002/lpor.202301399>.
- [28] Guan-Jie Huang, Hao-Yu Cheng, Yu-Lung Tang, Ikuto Hotta, Junichi Takahara, Kung-Hsuan Lin, and Shi-Wei Chu. Transient Super-/Sub-Linear Nonlinearities in Silicon Nanostructures. *Advanced Optical Materials*, 10(5):2101711, 2022. _eprint: <https://onlinelibrary.wiley.com/doi/pdf/10.1002/adom.202101711>.
- [29] Kentaro Nishida, Koki Sasai, Rongyang Xu, Te-Hsin Yen, Yu-Lung Tang, Junichi Takahara, and Shi-Wei Chu. All-optical scattering control in an all-dielectric quasi-perfect absorbing Huygens’ metasurface. *Nanophotonics*, 12(1):139–146, January 2023.

- [30] Anna Archetti, Ren-Jie Lin, Nathanaël Restori, Fatemeh Kiani, Ted V. Tsoulos, and Giulia Tagliabue. Thermally reconfigurable metalens. *Nanophotonics*, 11(17):3969–3980, September 2022. Publisher: De Gruyter.
- [31] Mikhail Y. Shalaginov, Sensong An, Yifei Zhang, Fan Yang, Peter Su, Vladimir Liberman, Jeffrey B. Chou, Christopher M. Roberts, Myungkoo Kang, Carlos Rios, Qingyang Du, Clayton Fowler, Anuradha Agarwal, Kathleen A. Richardson, Clara Rivero-Baleine, Hualiang Zhang, Juejun Hu, and Tian Gu. Reconfigurable all-dielectric metalens with diffraction-limited performance. *Nature Communications*, 12(1):1225, February 2021. Publisher: Nature Publishing Group.
- [32] Maxim R. Shcherbakov, Polina P. Vabishchevich, Alexander S. Shorokhov, Katie E. Chong, Duk-Yong Choi, Isabelle Staude, Andrey E. Miroshnichenko, Dragomir N. Neshev, Andrey A. Fedyanin, and Yuri S. Kivshar. Ultrafast All-Optical Switching with Magnetic Resonances in Nonlinear Dielectric Nanostructures. *Nano Letters*, 15(10):6985–6990, October 2015.
- [33] P. M. Fauchet and D. Hulin. Ultrafast carrier relaxation in hydrogenated amorphous silicon. *Journal of the Optical Society of America B*, 6(5):1024, May 1989.
- [34] Giuseppe Della Valle, Ben Hopkins, Lucia Ganzer, Tatjana Stoll, Mohsen Rahmani, Stefano Longhi, Yuri S. Kivshar, Costantino De Angelis, Dragomir N. Neshev, and Giulio Cerullo. Nonlinear Anisotropic Dielectric Metasurfaces for Ultrafast Nanophotonics. *ACS Photonics*, 4(9):2129–2136, September 2017.
- [35] Lin Chang, Songtao Liu, and John E. Bowers. Integrated optical frequency comb technologies. *Nature Photonics*, 16(2):95–108, February 2022. Publisher: Nature Publishing Group.
- [36] Oltjon Kodheli, Eva Lagunas, Nicola Maturo, Shree Krishna Sharma, Bhavani Shankar, Jesus Fabian Mendoza Montoya, Juan Carlos Merlano Duncan, Danilo Spano, Symeon Chatzinotas, Steven Kisseleff, Jorge Querol, Lei Lei, Thang X. Vu, and George Goussetis. Satellite Communications in the New Space Era: A Survey and Future Challenges. *IEEE Communications Surveys & Tutorials*, 23(1):70–109, 2021. Conference Name: IEEE Communications Surveys & Tutorials.
- [37] B.K. Nayak and M.C. Gupta. Femtosecond-laser-induced-crystallization and simultaneous formation of light trapping microstructures in thin a-Si:H films. *Applied Physics A*, 89(3):663–666, September 2007.
- [38] Jonas Berzinš, Simonas Indrišiūnas, Stefan Fasold, Michael Steinert, Olga Žukovskaja, Dana Cialla-May, Paulius Gečys, Stefan M. B. Bäumer, Thomas Pertsch, and Frank Setzpfandt. Laser-induced spatially-selective tailoring of high-index dielectric metasurfaces. *Optics Express*, 28(2):1539, January 2020.
- [39] Guntis Marcins, Jelena Butikova, Ivars Tale, Boris Polyakov, Robert Kalendarjov, and Aleksej Muhin. Crystallization processes of amorphous Si by thermal annealing and pulsed laser processing. *IOP Conference Series: Materials Science and Engineering*, 23:012035, June 2011.
- [40] J. D. Hoyland and D. Sands. Temperature dependent refractive index of amorphous silicon determined by time-resolved reflectivity during low fluence excimer laser heating. *Journal of Applied Physics*, 99(6):063516, March 2006.
- [41] G. Vuye, S. Fisson, V. Nguyen Van, Y. Wang, J. Rivory, and F. Abelès. Temperature dependence of the dielectric function of silicon using in situ spectroscopic ellipsometry. *Thin Solid Films*, 233(1):166–170, October 1993.
- [42] Nicolas Cherroret, Abhijit Chakravarty, and Aravinda Kar. Temperature-dependent refractive index of semiconductors. *Journal of Materials Science*, 43(6):1795–1801, March 2008.
- [43] Alfredo Naef, Ershad Mohammadi, Ted V. Tsoulos, and Giulia Tagliabue. Light-Driven Thermo-Optical Effects in Nanoresonator Arrays. *Advanced Optical Materials*, 11(20):2300698, 2023. _eprint: <https://onlinelibrary.wiley.com/doi/pdf/10.1002/adom.202300698>.
- [44] Min Hu and Gregory V. Hartland. Heat Dissipation for Au Particles in Aqueous Solution: Relaxation Time versus Size. *The Journal of Physical Chemistry B*, 106(28):7029–7033, July 2002. Publisher: American Chemical Society.

- [45] Khosro Zangeneh Kamali, Lei Xu, Nikita Gagrani, Hark Hoe Tan, Chennupati Jagadish, Andrey Miroshnichenko, Dragomir Neshev, and Mohsen Rahmani. Electrically programmable solid-state metasurfaces via flash localised heating. *Light: Science & Applications*, 12(1):40, February 2023. Publisher: Nature Publishing Group.
- [46] Kentaro Nishida, Po-Hsueh Tseng, Yu-Chieh Chen, Pang-Han Wu, Chi-Yin Yang, Jhen-Hong Yang, Wei-Ruei Chen, Olesiya Pashina, Mihail I. Petrov, Kuo-Ping Chen, and Shi-Wei Chu. Optical Bistability in Nanosilicon with Record Low Q -Factor. *Nano Letters*, 23(24):11727–11733, December 2023.
- [47] Yu-Lung Tang, Te-Hsin Yen, Kentaro Nishida, Junichi Takahara, Tianyue Zhang, Xiangping Li, Katsumasa Fujita, and Shi-Wei Chu. Mie-enhanced photothermal/thermo-optical nonlinearity and applications on all-optical switch and super-resolution imaging [Invited]. *Optical Materials Express*, 11(11):3608, November 2021.
- [48] Ted V. Tsoulos and Giulia Tagliabue. Self-induced thermo-optical effects in silicon and germanium dielectric nanoresonators. *Nanophotonics*, 9(12):3849–3861, September 2020.
- [49] Victor K. Pustovalov. Light-to-heat conversion and heating of single nanoparticles, their assemblies, and the surrounding medium under laser pulses. *RSC Advances*, 6(84):81266–81289, 2016. Publisher: Royal Society of Chemistry.
- [50] Guillaume Baffou. Anti-Stokes Thermometry in Nanoplasmonics. *ACS Nano*, 15(4):5785–5792, April 2021. Publisher: American Chemical Society.
- [51] Shen Xu, Aoran Fan, Haidong Wang, Xing Zhang, and Xinwei Wang. Raman-based Nanoscale Thermal Transport Characterization: A Critical Review. *International Journal of Heat and Mass Transfer*, 154:119751, June 2020.
- [52] T. R. Hart, R. L. Aggarwal, and Benjamin Lax. Temperature Dependence of Raman Scattering in Silicon. *Physical Review B*, 1(2):638–642, January 1970. Publisher: American Physical Society.
- [53] George P. Zograf, Mihail I. Petrov, Dmitry A. Zuev, Pavel A. Dmitriev, Valentin A. Milichko, Sergey V. Makarov, and Pavel A. Belov. Resonant Nonplasmonic Nanoparticles for Efficient Temperature-Feedback Optical Heating. *Nano Letters*, 17(5):2945–2952, May 2017. Publisher: American Chemical Society.
- [54] George P. Zograf, Daniil Ryabov, Viktoria Rutckaia, Pavel Voroshilov, Pavel Tonkaev, Dmitry V. Permyakov, Yuri Kivshar, and Sergey V. Makarov. Stimulated Raman Scattering from Mie-Resonant Subwavelength Nanoparticles. *Nano Letters*, 20(8):5786–5791, August 2020. Publisher: American Chemical Society.
- [55] Mor Pal Vikram, Kentaro Nishida, Chien-Hsuan Li, Daniil Riabov, Olesiya Pashina, Yu-Lung Tang, Sergey V. Makarov, Junichi Takahara, Mihail I. Petrov, and Shi-Wei Chu. Photo-thermo-optical modulation of Raman scattering from Mie-resonant silicon nanostructures. *Nanophotonics*, 13(18):3581–3589, August 2024.
- [56] D. M. Bhusari, A. S. Kumbhar, and S. T. Kshirsagar. Temperature-dependent Raman studies of hydrogenated-amorphous-silicon films. *Physical Review B*, 47(11):6460–6464, March 1993. Publisher: American Physical Society.
- [57] G. Viera, S. Huet, and L. Boufendi. Crystal size and temperature measurements in nanostructured silicon using Raman spectroscopy. *Journal of Applied Physics*, 90(8):4175–4183, October 2001.
- [58] Lauren Zundel, Kellen Malone, Luis Cerdán, Rosario Martínez-Herrero, and Alejandro Manjavacas. Lattice Resonances for Thermoplasmonics. *ACS Photonics*, 10(1):274–282, January 2023. Publisher: American Chemical Society.
- [59] Rongyang Xu and Junichi Takahara. Radiative loss control of an embedded silicon perfect absorber in the visible region. *Optics Letters*, 46(4):805–808, February 2021. Publisher: Optica Publishing Group.
- [60] Rasoul Alaee, Mohammad Albooyeh, and Carsten Rockstuhl. Theory of metasurface based perfect absorbers. *Journal of Physics D: Applied Physics*, 50(50):503002, November 2017. Publisher: IOP Publishing.

- [61] Raphael Tsu and Jesus Gonzalez Hernandez. Temperature dependence of silicon Raman lines. *Applied Physics Letters*, 41(11):1016–1018, December 1982.